PHYSICS

Reconstructive spectrometer using double-layer disordered metasurfaces

Dong-gu Lee†, Gookho Song†, Chunghyung Lee, Chanseok Lee, Mooseok Jang*

Conventionally, optical spectrometers rely on traditional dispersive elements like grating and prism, which pose inherent challenges for miniaturizing spectrometers, including the trade-off between propagation distance and spectral resolution and calibration ambiguity. Here, we present a random dispersive element—double-layer disordered metasurfaces—where wavelength-specific speckle patterns can be uniquely determined a priori without ambiguity in wavelength and propagation distance. By directly mounting this element on an image sensor, we implement a spectrometer with a spectral resolution of around 1 nanometer and an operable range of 440 to 660 nanometers, comprising 221 spectral channels, within a form-factor of less than 1 centimeter. Our results firmly establish that the versatility of multilayer disordered metasurfaces in the spatio-spectral domain can be fully exploited for on-sensor spectroscopic applications.

INTRODUCTION

Over the past few decades, there has been a growing demand for small form-factor spectrometers (*1*), enabling on-site and real-time material characterization and chemical analysis across various scientific and industrial fields. Typically, spectrometers rely on conventional dispersive components—optical grating and prism—where these components diffract or refract the light beams into different angles corresponding to their wavelengths. This operating principle requires an additional relaying optical system or free propagation distance for angle-to-position conversion so that the different wavelength components can be sampled with a sensor array. With the traditional components, it is challenging to simultaneously achieve the features of small form-factor and high spectral resolving power as the spatial separation of nearby wavelengths (i.e., the inverse of the spectral resolution), which is proportional to the path length Lwithin a spectrometer. Furthermore, the inherent ambiguity between free-space distance and incoming wavelength necessitates frequent calibration of the one-to-one mapping relation between spectral and spatial domains to ensure diffraction-limited performance.

Toward the goal of achieving miniaturized spectrometers, there have been tremendous research efforts to overcome the aforementioned limitations (*2*–*5*), including advanced narrow-band filter designs (*6*–*8*), on-chip interferometers (*9*–*11*), and reconstructive spectrometers (*12*–*16*). Unlike conventional spectrometers that rely on a one-to-one mapping where each sensor element directly measures the intensity of a specific spectral band, reconstructive approaches involve a complex spectral-to-spatial mapping where the entire spectral information is sampled with a sensor array on a random basis and is subsequently decoded on the basis of the linear mapping relation. Often, reconstructive spectrometers use diffusive media to achieve the complex mapping within the spatio-spectral domain (*17*–*25*), generating wavelength-specific speckle patterns with their spectral resolution inversely proportional to L^2 (*26*). This characteristic makes the reconstructive approach one of the most promising paradigms for achieving a high spectral resolution and a large operational range with the additional benefit of ease of integration. Notably, at the limit of high spectral resolution around 1 nm, spectrometers based on narrow-band filters become highly inefficient, rejecting most of the incoming light, and on-chip interferometers become extremely sensitive to mechanical and thermal noise, which can easily cause path length variations exceeding 1 nm.

Unfortunately, the reconstructive approaches require exhaustive characterization, involving the measurement of a library of wavelength-specific speckle patterns for incoming light that can be tuned across the entire operational spectrum with a narrow linewidth. When the input-output relation is altered because of conformational changes in scatterers or external perturbations, this characterization has to be performed repeatedly for the entire spectrum. Combined with the demanding requirements of high-performance lasers, this nonpredictable calibration scheme serves as a key prohibitive factor for realizing reconstructive spectrometers suitable for practical applications, especially when aiming for both a wide operational spectrum and high spectral resolution (i.e., a large number of resolvable spectral bands). Using a thin, forward-scattering medium for spectral-to-spatial mapping, this calibration process can be relatively simplified on the basis of a chromato-axial memory effect where the same speckle pattern magnifies or demagnifies depending on the incoming wavelength (*27*). However, in this regime where light propagation can be approximated with a single diffractive layer, akin to conventional spectrometers, it inherits the same limitations of the trade-off between form factor and spectral resolution and the degeneracy between wavelength and path length.

Here, we report the use of double-layer disordered metasurfaces (*28*) as a spatio-spectral mixer, providing a versatile complex mapping characteristic of high spectral sensitivity within a small footprint of 1 cm. The double-layer disordered metasurfaces provide two features—predictability and definitive mapping—that are particularly useful in implementing the spectrometer. We have shown that the spectral response of the double-layer disordered metasurfaces is seemingly random but uniquely and accurately describable on the basis of the preconfigured design of disordered meta-atoms and a set of configurational parameters. To validate the usability of the computer-generated spatio-spectral responses, we have implemented a reconstructive spectrometer by directly mounting the double-layer disordered metasurfaces on a conventional image sensor and demonstrated the retrieval of the entire visible spectrum with a spectral sensitivity of 1 nm (Fig. 1).

Department of Bio and Brain Engineering, Korea Advanced Institute of Science and Technology (KAIST), Daejeon 34141, South Korea.
*Corresponding author. Email: mooseok@kaist.ac.kr
†These authors contributed equally to this work.

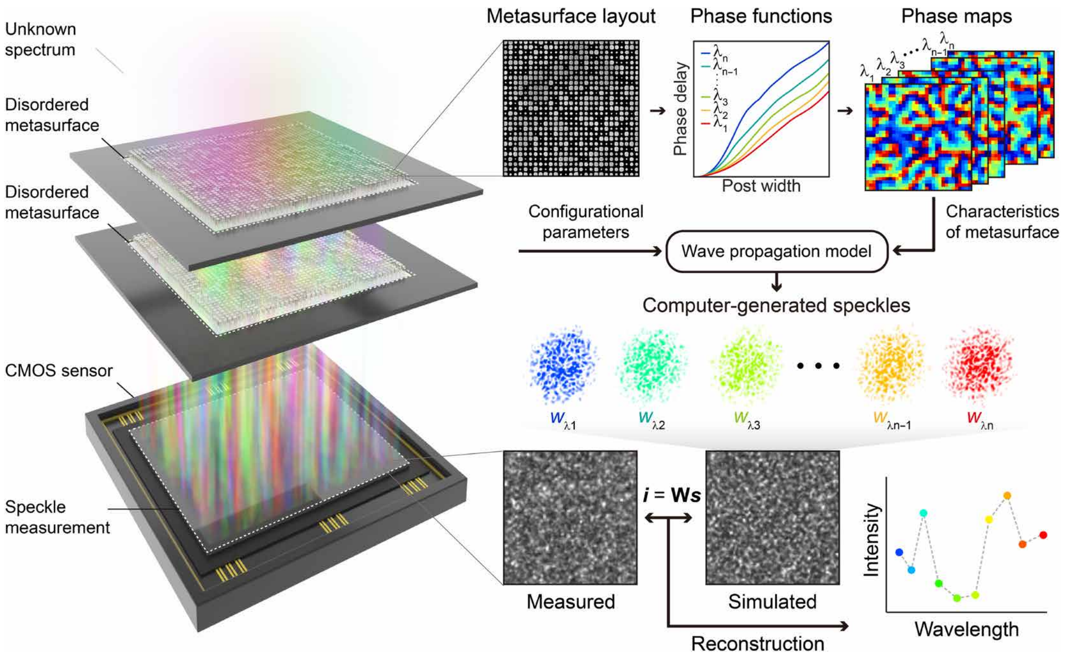

Fig. 1. Schematic of reconstructive spectrometer based on double-layer disordered metasurfaces. The in-line spectrometer consists of double-layer disordered metasurfaces and a CMOS sensor. The disordered metasurface serves as a random dispersive element that generates wavelength-specific speckle patterns. The measured intensity map can thus be represented as the superposition of speckle patterns on the basis of independent spectral channels. The design of disordered metasurfaces and the configurational parameters are used to construct the computer-generated speckle library, which is subsequently used to reconstruct the spectrum by solving the inverse problem represented as matrix-vector multiplication, $\mathbf{i} = \mathbf{Ws}$, where $\mathbf{i}$ is the vectorized measured intensity, $\mathbf{W}$ is spectral response matrix, and $\mathbf{s}$ is the input spectrum.

RESULTS

Spectral response of disordered metasurfaces

As shown in Fig. 2A, we fabricated disordered metasurfaces with silicon nitride (SiN_x) nanoposts of randomized widths, with associated phase delay values ranging from 0 to 2π at the design wavelength of 532 nm (see Materials and Methods for details on the design and fabrication of the disordered metasurface) (*29*). The fabricated metasurfaces were directly mounted on top of an image sensor, as depicted in the schematic configuration in Fig. 2B. Before investigating the spectral characteristics of the disordered metasurface, we first measured the phase delay values through the patches of nanoposts with uniform widths ranging from 60 to 300 nm using a custom-built off-axis holographic microscope. As shown in Fig. 2 (C and D), the measured phase delay values were notably reduced at longer wavelengths, closely matching with the simulated values obtained by rigorous coupled-wave analysis (RCWA). Notably, as the wavelength increases, the effective index of refraction decreases much more rapidly than dictated by the inherent material dispersion. Nevertheless, the spectral resolution achievable by this dispersion effect alone is insufficient for implementing a spectrometer, resulting in spectral resolutions around 175 nm for SiN_x nanoposts and 50 nm for c-Si nanoposts (see fig. S1 for spectral correlation profiles in a single-layer configuration without additional propagation distance).

The proposed spectrometer consists of two components—a random dispersive element composed of two layers of disordered metasurfaces and a two-dimensional (2D) image sensor (Fig. 2B)—arranged in an on-axis configuration, unlike a traditional spectrometer, where the sensor array is positioned off-axis to sample specific diffraction orders. When stacking two metasurfaces in front of an image sensor, there are two major variables, T and L, the thickness of the random dispersive element composed of the two metasurfaces and the element-to-sensor distance, respectively. Those two variables determine the spectral resolution, $\delta\lambda$, and the sampling condition for speckles in conjunction with the additional variables such as the aperture size of disordered metasurfaces, D, and the pixel size of the image sensor, Δp.

A disordered metasurface can be considered as a random spatial mixer that simultaneously generates many plane wave components within a confined spatial frequency range. Because of the angular dispersion effect, the interfering plane waves with random phases generate a wavelength-dependent speckle pattern when given sufficient propagation distance. Then, the spectral resolution, $\delta\lambda$, can be defined as the full-width at half maximum (FWHM) of the spectral correlation profile for the generated speckle patterns. Considering the λ-derivative of the relative optical phase delay in between plane wave components propagating over the distance of L (*30*), the spectral resolution for single-layer disordered metasurface can be described by

$$\delta\lambda \approx \frac{\lambda^2}{2L\left(1-\cos\theta_{ms}\right)} \tag{1}$$

where θ_{ms} is the highest acceptance angle, $\theta_{ms} = \tan^{-1}\left(\frac{D}{2L}\right)$, and λ is the reference wavelength (see text S1 for the derivation of analytical formula of $\delta\lambda$). When L is excessively larger than D, $\delta\lambda$ increases proportionally to L (i.e., $\delta\lambda \sim \frac{4\lambda^2}{D^2}L$ with the paraxial approximation) due to the loss of high transverse wave vector components. On the

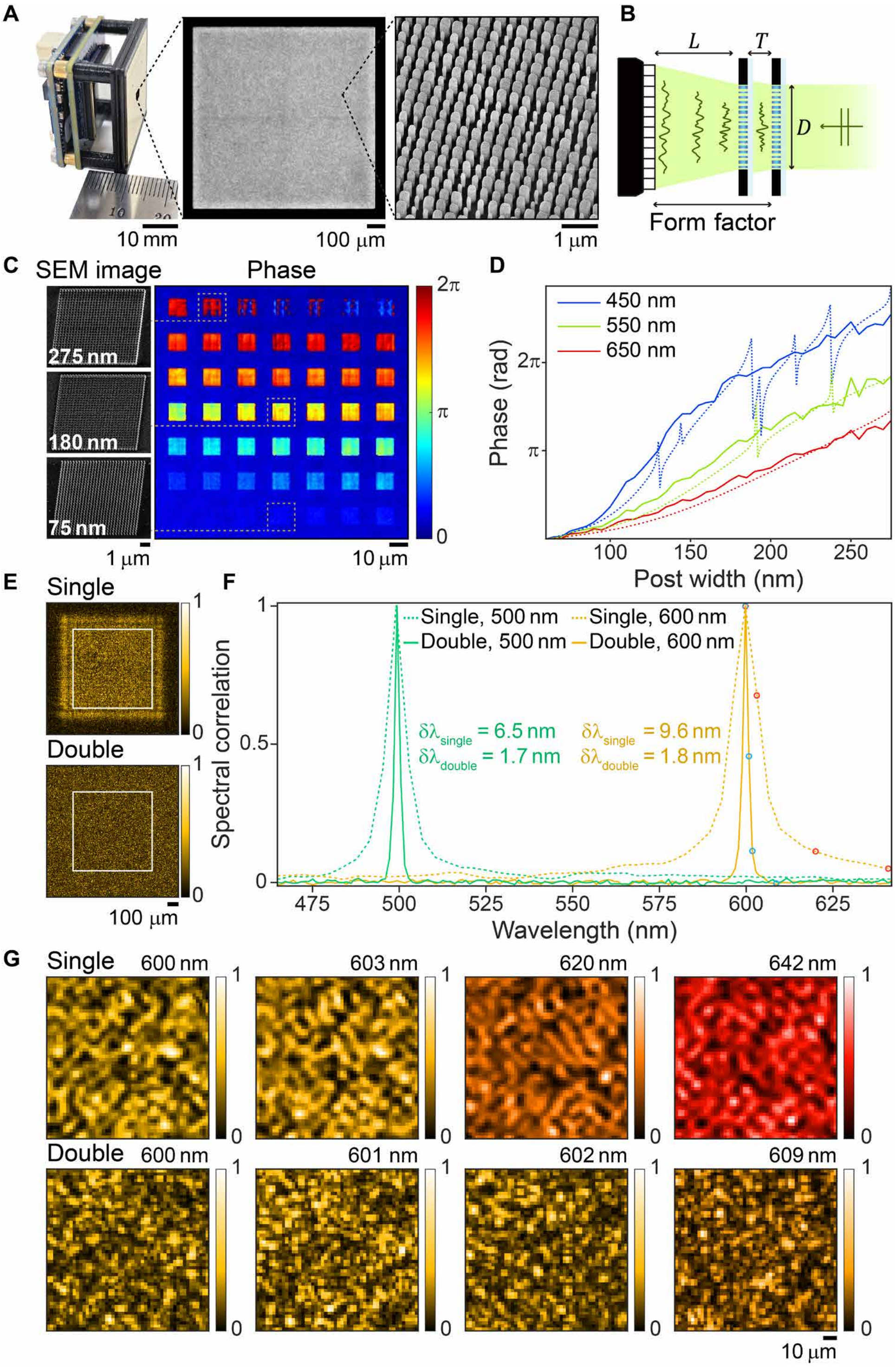

Fig. 2. Spectral characteristics of the double-layer disordered metasurfaces. (**A**) Photograph of a disordered metasurface-based spectrometer in on-sensor configuration and SEM image of a fabricated metasurface. (**B**) Schematic spectrometer configuration. The key parameters that determine the spectral resolution are the thickness of the random dispersive element, *T*, the element-to-sensor distance, *L*, and the aperture size, *D*. (**C**) Phase delay map of the fabricated patches of metasurface measured via off-axis holography at a 550-nm wavelength with representative SEM images. Each fabricated patch has an identical post width set to 60 to 300 nm with 5-nm spacing from bottom left to top right. (**D**) Wavelength-dependent phase of transmitted light versus post width. Solid lines indicate the measured values, while the dotted lines indicate the simulated values derived from RCWA. (**E**) Measured speckle patterns for single- and double-layer disordered metasurface. The white squares indicate the sensing area. (**F**) Spectral speckle correlation profiles for the reference speckle map measured at the wavelengths of 500 and 600 nm. (**G**) Measured speckle patterns at the representative wavelengths along decorrelation profiles in (F), indicated as red and blue circles, respectively, for single- and double-layer disordered metasurface.

other hand, when L approaches zero, the effect of the acceptance angle becomes marginal, resulting in $\delta\lambda \sim \frac{\lambda^2}{2L}$. Consequently, $\delta\lambda$ exhibits a local minimum for L around $0.4D$.

However, this ideal spectral resolution is not practically achievable, considering that the wavelength and the acceptance angle also determine the speckle size on the sensor array. More specifically, the speckle size, Δs, is given as $\frac{\lambda}{2\mathrm{NA}_{\mathrm{eff}}}$ where the effective numerical aperture, $\mathrm{NA}_{\mathrm{eff}}$, is given as $\sin\theta_{ms}$ (*31*, *32*). In the visible regime, Δs can be as small as ~300 nm at the spectral width minimum condition of $L = 0.4D$. To fully use the information contained in the captured speckle pattern for spectrum reconstruction, the speckle contrast and the background speckle correlation should be close to 1 and 0, respectively. This sampling condition is met when the speckle size, Δs, is around the size of a single pixel, Δp (fig. S2), imposing an additional requirement on the ratio, D/L, and limiting achievable spectral resolution in a single-layer scheme.

With an additional layer of disordered metasurface, the λ-derivative of the relative optical phase delay in between plane wave components is increased because of the additional scattered path lengths. For the double-layer disordered metasurfaces, the spectral resolution can be described by

$$\delta\lambda \approx \frac{\lambda^2}{2} \frac{1}{T\left(1-\cos\theta_{mm}\right) + L\left(1-\cos\theta_{ms}\right)} \tag{2}$$

where θ_{mm} is the highest acceptance angle from the perspective of the rear layer, $\theta_{mm} = \tan^{-1}\left(\frac{D}{2T}\right)$. This relation indicates that, by introducing an additional disordered metasurface, the challenge for the single-layer scheme (i.e., restriction in setting θ_{ms}) in achieving a high spectral resolution can be resolved. More specifically, with the asymmetric setting of $T \sim 0.4D$ and $T < L$, we can decouple the criteria on spectral resolution and sampling condition, which allows us to achieve a high spectral resolution and a small form factor simultaneously.

In our study, we determined $D = 1$ mm, $T = 1.34$ mm, $L = 8$ mm considering the image sensor parameters of $\Delta p = 2.4$ μm and sensing area $= 0.5\ \mathrm{mm}^2$. The expected features of the interplay between spectral resolution and system parameters were confirmed with numerical simulation (fig. S3). Figure 2 (E and F, respectively), presents the measured speckle patterns and the spectral correlation profile through single- and double-layer configuration with the same form factor (i.e., single-layer configuration with $L = 9.34$ mm). At the center wavelengths of 500 and 600 nm, we confirmed that the spectral resolution was notably improved in the double-layer structure with 1.7 and 1.8 nm, compared to 6.5 and 9.6 nm for the single layer (see Materials and Methods for detailed optical setup). Notably, the undesired 0th order diffraction pattern leads to a high background correlation in the single layer despite the presence of an aperture (see fig. S4 for a detailed explanation of the effect of the aperture). In contrast, the representative speckle patterns measured at $\lambda = 600$ nm to $\lambda = 609$ nm through a double layer show that the speckle patterns are decorrelated in a randomized manner, resulting in the background correlation value close to 0 (Fig. 2G).

Mapping ambiguity for input wavelengths and propagation distances

In addition to the limit in spectral resolution, a single-layer metasurface presents a critical drawback as a spectroscopic element: the common degeneracy problem of the single diffractive element, where the same intensity pattern can be generated by multiple combinations of wavelengths, λ, and element-to-sensor distance, L. Figure 3A presents the correlation values between the reference speckle pattern measured at a wavelength ($\lambda_{\mathrm{ref}} = 550.8$ nm) and element-to-sensor distance ($L_{\mathrm{ref}} = 9.5$ mm) and the speckle patterns measured at various wavelength (λ_{mea}) and element-to-sensor distance (L_{mea}). As expected from the Fresnel diffraction formula and the dispersion relation given in Fig. 2D, the speckle patterns expand or contract with varying λ and L at a linear rate (i.e., locally, the speckle pattern

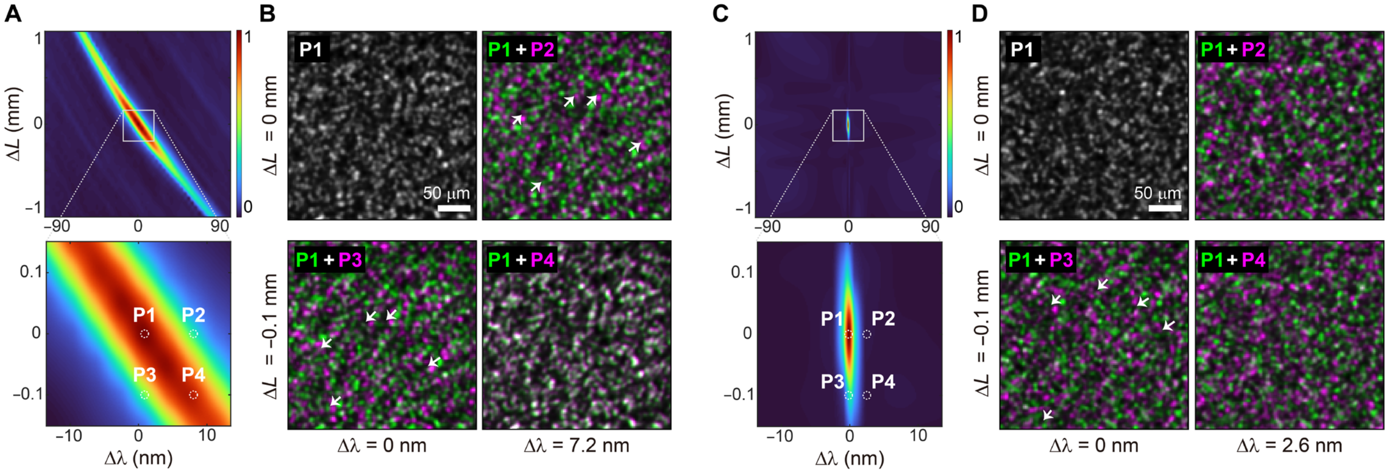

Fig. 3. Characterization of speckle correlation for input wavelength and sensor-to-element distance. (**A**) Measured correlation map for single-layer disordered metasurface. Peak values of the cross-correlation of the reference speckle pattern measured at $\lambda_{\mathrm{ref}} = 550.8$ nm and $L_{\mathrm{ref}} = 9.5$ mm with the speckle patterns measured at various wavelength, $\lambda_{\mathrm{mea}} = \lambda_{\mathrm{ref}} + \Delta\lambda$, and sensor-to-element distance, $L_{\mathrm{mea}} = L_{\mathrm{ref}} + \Delta L$. (**B**) Measured speckle patterns at ($\Delta\lambda$ [nm], ΔL [mm]) = (0, 0), (7.2, 0), (0, −0.1), and (7.2, −0.1) marked as white circles in (A). The speckle patterns (magenta), for the cases of $\Delta\lambda \neq 0$ or $\Delta L \neq 0$, are overlaid with the reference speckle pattern (green) to visualize the effect of the chromato-axial memory effect. The white arrows indicate the displacement of speckle granules. (**C**) Measured correlation map for double-layer disordered metasurfaces for the same λ_{ref} and L_{ref} as in (A). (**D**) Measured speckle patterns at ($\Delta\lambda$ [nm], ΔL [mm]) = (0, 0), (2.6, 0), (0, −0.1), and (2.6, −0.1) marked as white circles in (C).

translates as shown in Fig. 3B). Therefore, a set of λ and L, resulting in high correlation values, follows a hyperbolic trend. The peak correlation values along this hyperbolic profile were larger than 0.5 even for the wavelength deviation, $\Delta\lambda = |\lambda_{\text{ref}} - \lambda_{\text{mea}}|$, of more than 50 nm. Similar to the miscalibration issue in dispersive spectrometers, this degeneracy renders the system highly vulnerable to optical misalignments and often leads to inaccurate estimation on absolute wavelength, necessitating frequent calibration procedures.

For the double-layer metasurfaces, however, in contrast to the single-layer case, a completely different speckle pattern emerges for $\Delta\lambda$ exceeding the spectral resolution of the double-layer metasurfaces, resulting in the unique correlation peak at the specific combination of $\Delta\lambda = \Delta L = 0$ (Fig. 3, C and D). This effect can be understood by the operation of double-layer metasurfaces where the speckle pattern generated by the front layer is further modulated by random phase delay imparted on the rear layer. Consistent with this interpretation, correlation peaks were observed for the specific condition where the thickness variation of the random dispersive element, ΔT, and the element-to-sensor distance variation, ΔL, satisfy the specific ratio of $\Delta T/\Delta L$ within a limited spectral range (fig. S5). Because the likelihood that T and L satisfy such specific conditions is extremely low, double-layer metasurfaces effectively resolve the degeneracy issue in diffractive spectroscopy.

Predictability of the spectro-spatial response of double-layer disordered metasurfaces

The speckle output at a specific wavelength and configuration can be predicted through a parameterized wave propagation model (Fig. 4, A and B; see Materials and Methods for implementation of wave propagation model). The phase delay map, representing the 2D phase modulation of the metasurface, was obtained by mapping the meta-atom width distribution (i.e., the design of the disorder-engineered metasurface) to the corresponding phase delay values. These values were derived from RCWA simulations under normal incidence conditions at each wavelength, accounting for material dispersion effects. The amplitude map was assumed to be uniform.

With a numerical model, we first confirmed the required accuracy to realize predictive capability on wavelength-sensitive speckle patterns generated through double-layer metasurfaces. For a spectrometer based on double-layer disordered metasurfaces, there are additional configurational parameters such as Δx_{mm}, Δy_{mm}, $\Delta\theta_{mm}$, Δx_{ms}, Δy_{ms}, and $\Delta\theta_{ms}$, besides the thickness of the random dispersive element, T, and element-to-sensor distance, L. Δx_{mm}, Δy_{mm}, and $\Delta\theta_{mm}$, respectively, indicate the amount of translational shifts and in-plane rotation in between two disordered metasurfaces. Meanwhile, Δx_{ms}, Δy_{ms}, and $\Delta\theta_{ms}$, respectively, describe the same configurational parameters in between the rear metasurface and the sensor array. We calculated the resulting speckle pattern at the sensor using the wavelength-dependent phase delay maps at the reference wavelength of 500 nm with varying optical configurations of the spectrometer. The sensitivity of configurational parameters (i.e., FWHM of speckle intensity correlation profile for a certain parameter) was estimated as 770 nm for Δx_{mm} and Δy_{mm}, 0.118° for $\Delta\theta_{mm}$, 3.1 μm for T, and 135 μm for L (fig. S6). The effect of tip/tilt of metasurfaces can be neglected within a range of a few degrees because of the large angular memory effect range of disordered metasurfaces where a transmitted wavefront is tilted by the same angle as a coherent beam incident on a disordered medium (*28*, *33*, *34*) [i.e., low angular sensitivity of the nanoposts' resonances (*35*)].

Ideally, a set of configurational parameters can be found by maximizing the correlation between the measured speckle and the numerically generated speckle. However, because of the high sensitivity of the speckle patterns to the translational and rotational parameters on the order of 1 μm and 0.1°, it is practically impossible to identify the parameter set in a brute-force manner. To address this issue, we implemented a Bayesian optimization module with a Gaussian process surrogate model to correct all parameters simultaneously to maximize the correlation between the two speckle maps at reasonable computational costs (Fig. 4C). While the calibration wavelength was 620 nm, the correlation values were concurrently increased at other wavelengths like 500 nm over the iterations, indicating that the calibration procedure at a single wavelength can be comprehensively applied across all wavelengths. As shown in Fig. 4D, the identified configurational parameters exhibit a matched correlation peak at both on- and off-calibration wavelengths (i.e., 620 and 500 nm), indicating that they represent a unique parameter set corresponding to the physical configuration (i.e., global maxima for correlation values).

Figure 4 (E and F) presents the measured and simulated speckle maps with their 2D cross-correlation maps. The maximized correlation values for 620 and 500 nm inputs were around 0.3. This reduced correlation value can be attributed to system model mismatch, particularly variations in the optical response of dielectric nanoposts at high incidence angles reaching the rear metasurface, as well as reflections within the double-layer structure and the presence of 0th order components. Also, the estimated phase delay map could not be perfectly accurate because of fabrication errors on the nanoscopic scale. Nevertheless, in a magnified view of speckle patterns shown in Fig. 4 (E and F), the correspondence between measured and simulated speckle patterns is clearly observable at the off-calibration wavelength of 500 nm as well as the on-calibration wavelength of 620 nm, indicating the unique feature of the proposed spectrometer scheme based on double-layer disordered metasurfaces, where a single calibration can predict speckle patterns across entire spectral channels. These results indicate that our prediction scheme has practical tolerance to errors in phase delay maps caused by experimental imperfections (see fig. S7 for the effect of errors in phase delay functions versus meta-atoms, and see fig. S8 for the effect of stochastic errors in phase delay maps). The degree of tolerance to fabrication errors could be highly varying depending on the specific design of disordered metasurfaces, considering errors such as those caused by proximity effects in electron beam lithography and the collapse of high aspect ratio structures.

In the proposed speckle prediction scheme, additional parameters can be incorporated as variables in the Bayesian optimizer. For instance, to accommodate changes in the incidence angle, which notably affect the speckle pattern on a scale of 0.01°, the phase profile of the input beam can be parameterized by the incidence angles to the x and y axes and identified using the optimizer (see fig. S9 for the effect of incidence angle on speckle prediction). Furthermore, incorporating the incoming wavelength as a variable in the Bayesian optimizer could provide a potential route for the self-calibration of a source with an unknown wavelength.

Spectrum reconstruction using computer-generated speckle library

To demonstrate the capability of identifying absolute wavelength, we measured monochromatic speckle patterns at nine different

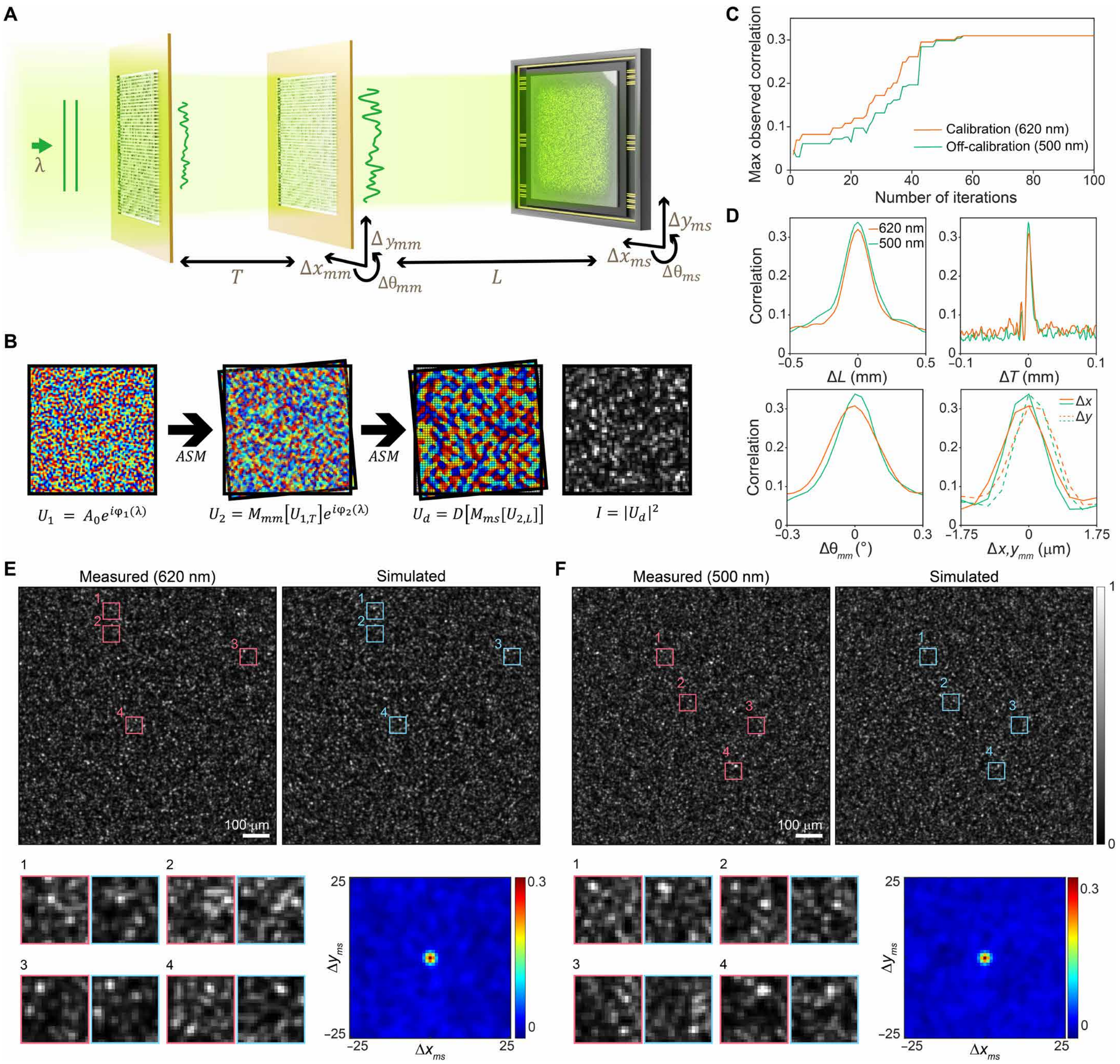

Fig. 4. Model-based prediction of wavelength-dependent speckle patterns. (**A**) Schematic of the optical configuration. (**B**) Schematic of wave propagation model for computer-generated speckle patterns. (**C**) Correlation coefficient profile between the measured and the computer-generated speckle patterns for each iteration of the optimization loop for on- and off-calibration wavelengths of 620 and 500 nm. (**D**) Correlation coefficient profiles between the measured speckle pattern and the simulated speckle patterns with varying configurational parameters. (**E** and **F**) Measured and simulated speckle patterns, respectively, at the on- and off-calibration wavelengths. The red and blue patches indicate the region for the zoom-in views. The cross-correlation maps between the measured and simulated speckle patterns are shown at the bottom right of (E) and (F).

wavelengths and compared them with the wavelength-dependent speckle library generated within a spectral range of 440 to 660 nm with 1-nm spacing (Fig. 5, A and B). Figure 5 (C and D) shows that the unique correlation peaks appear at a single spectral channel and the peak wavelength is identical to the absolute wavelength measured from a high-accuracy wavemeter, within a deviation of δλ.

For general spectral inputs, the intensity map can be considered as the weighted sum of spectral speckles, expressed as $I(\mathbf{r}) = \int W(\mathbf{r}, \lambda)S(\lambda)d\lambda$, where $\mathbf{r}$ is the position on an image sensor, $S(\lambda)$ is the input power of specific wavelength λ, and $W(\mathbf{r}, \lambda)$ is the spectral response at $\mathbf{r}$ for λ. With a discretized representation, the relation can be expressed as the system of linear equations, $\mathbf{i} = \mathbf{W}\mathbf{s}$,

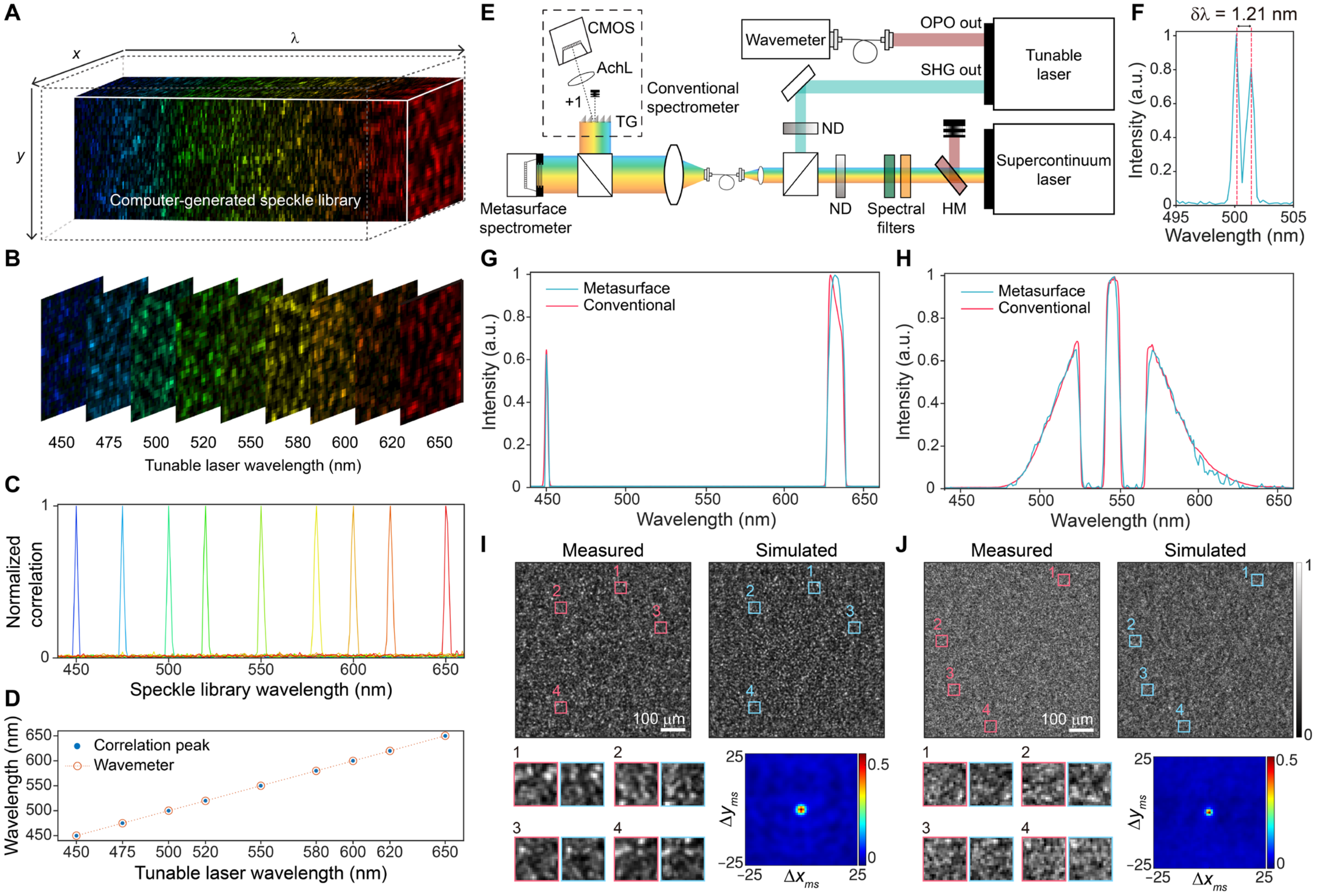

Fig. 5. Retrieval of input wavelength and spectrum using computer-generated speckle library. (**A**) Schematic of the computer-generated speckle library. (**B**) Measured speckle patterns from a monochromatic tunable laser. (**C**) Correlation coefficient profiles between measured speckle maps and computer-generated speckle library. Each curve is colored on the basis of the incoming wavelength. (**D**) Comparison of the retrieved wavelength and the absolute wavelength characterized with a commercial wavemeter. (**E**) Schematic of an optical setup for testing under various spectral inputs. AchL, achromatic lens; OPO, optical parametric oscillator; SHG, second harmonic generator; TG, transmission grating; HM, hot mirror; ND, neutral density filter. (**F**) The reconstructed spectrum for two adjacent spectral lines. The red dotted lines mark the readout from the commercial wavemeter. (**G** and **H**) The reconstructed spectra from the metasurface spectrometer and the conventional spectrometer, respectively, for the input spectrum composed of a monochromatic line at 450 nm and a continuous spectrum of a transmission filter with the center wavelength of 630 nm and for the input spectrum of a continuous spectrum in visible range filtered by two notch filters. (**I** and **J**) Measured and simulated speckle patterns for the input spectra of (G) and (H), respectively. The red and blue patches indicate the region for the zoom-in views. The cross-correlation maps between the measured and simulated speckle patterns are shown at the bottom right of (I) and (J). a.u., arbitrary units.

where $\mathbf{i}$ is a vector representing measured intensity at each pixel of the sensor and $\mathbf{s}$ is a vector representing the discretized input spectrum. $\mathbf{W}$ is a spectral response matrix where each column describes the intensity values of vectorized speckle output at a specific wavelength. In our reconstruction scheme, $\mathbf{W}$ is derived from the numerically generated speckle library, with the dimension of 221 columns and 300 × 300 rows (i.e., the number of camera pixels used for reconstruction).

To demonstrate the reconstruction of arbitrary spectrum inputs, an input spectrum was synthesized with tunable and supercontinuum lasers of monochromatic and continuous-spectral characteristics (as shown in Fig. 5E; see Materials and Methods for detailed optical setup). The spectrum $\mathbf{s}$ is reconstructed from the measured intensity $\mathbf{i}$ by solving the system of linear equations, $\mathbf{i} = \mathbf{W}\mathbf{s}$, with the gradient descent optimization method (see Materials and Methods for detailed reconstruction method).

First, as shown in Fig. 5F, we verified the spectrometer's ability to resolve two adjacent spectral lines separated by 1.21 nm (see fig. S10 for more detailed results). Then, we tested the spectrometer performance for two spectrum inputs—(i) a hybrid spectrum of discrete and continuous spectral inputs at two extreme wavelengths (i.e., monochromatic input at 450 nm and a continuous spectrum of a spectral filter with the center wavelength of 630 nm) and (ii) a continuous spectrum of ~100-nm width filtered by two notch filter, presented in Fig. 5 (G and H). Such accurate reconstruction results under diverse input spectrum conditions indicate that the spatial information captured from a commercial image sensor can preserve information within each narrow spectral channel even in a situation where a large number of independent speckle maps from a broad bandwidth spatially overlap (see fig. S11 for the numerical analysis on the reconstruction performance under stochastic errors in phase delay maps). This aspect was further confirmed by the correspondence between the measured speckle and the reconstructed speckle patterns for broad spectra (Fig. 5, I and J).

DISCUSSION

Here, we have presented a reconstructive spectrometer using the double-layer disordered metasurfaces that overcomes the fundamental limitations of conventional spectrometer designs based on a single diffractive layer—(i) the trade-off limit in spectral resolution and form factor and (ii) the mapping ambiguity for input wavelengths and propagation distances. Our study extends the engineering domain of the disordered metasurface platform into the spatio-spectral domain, resolving the major challenges of reconstructive spectrometers—the need for exhaustive calibration of output speckles for all independent spectral inputs. On the basis of those features, we have demonstrated the characterization of absolute incoming wavelength and the reconstruction of continuous spectra, with a spectral resolution of around 1 nm over the entire visible spectrum of 440 to 660 nm, based only on a computer-generated library of wavelength-dependent speckle maps. The proposed on-sensor configuration, consisting of the dispersive element (i.e., double-layer disordered metasurfaces) directly mounted on an image sensor, makes it ideal for achieving robust spectrum reconstruction performance in a cost-effective manner as well as providing both ease of integration and small form factor compatible to mobile devices.

The proposed spectrometer offers additional unique advantages based on its structure and operating principle. First, the dispersive property is predominantly determined by angular dispersion, allowing the operable spectral range to be easily extended to an even wider spectral range. While our demonstration was carried out at visible regime, the proposed scheme is fully capable of implementing a spectrometer with a working range of 400 to 1100 nm (see fig. S12 for the demonstration of the wavemeter operating in the near-infrared range of 900 to 1100 nm using a disordered metasurface). Second, this configuration is robust against fabrication imperfections, as well as mechanical and thermal fluctuations. Unlike resonance-based approaches, the location of the correlation peak between the measured and computer-generated speckle maps (i.e., estimated wavelength) remains unaffected by fabrication errors in individual meta-atoms on the scale of tens of nanometers. Third, the double-layer configuration is characterizable with a handful of nondegenerate parameters, enabling seamless incorporation with computational optimization techniques. Unlike conventional spectrometers, this feature will eliminate the need for frequent physical calibration of spectrometers that require additional sources with known wavelengths.

The spectral performance of the proposed spectrometer can be further improved by simply adjusting configurational parameters, such as D, T, and L. While our demonstration is limited to $D = 1$ mm, an aperture size of D greater than 10 mm would result in a spectral resolution of less than 0.1 nm with the form factor, $T + L$, of less than 1 cm (fig. S13). Also, by introducing a few additional layers of disordered metasurfaces, the spectral resolution can be further improved with a marginal increase in the overall form factor (see text S1 for the derivation of the relationship between the number of layers and spectral resolution). The spectral resolution and the speckle contrast can also be further enhanced by using high-index dielectric materials, such as c-Si and TiO_2. Although the choice of complementary metal-oxide semiconductor (CMOS) detector does not substantially affect the spectral resolution, the overall form factor of the spectrometer can be notably reduced by using a CMOS detector with a smaller pixel size (see text S2 for detailed descriptions of how the detector's properties affect the spectrometer's performance).

Another important aspect in the design perspective is the light throughput through disordered structures. With the close-to-unity transmittance for a single metasurface, the light transmittance through two disordered metasurfaces was measured to be around 32% at the wavelength of 532 nm, and around 1% of the incoming power was used for spectrum retrieval, which is remarkably high compared to conventional diffusive media used in the reconstructive spectrometer, albeit lower than commercial spectrometers. With this signal throughput, our experiments could be conducted under practical settings with an average incident power of 10 μW and an exposure time of 10 ms (see text S3 for photon budget analysis). However, because of the process of decoding the spectral speckle pattern from each independent spectral channel within a superimposed speckle pattern, the signal-to-noise ratio (SNR) of the proposed reconstructive approach is $\sqrt{N_s}$ times lower than that of a conventional dispersive spectrometer, where N_s represents the number of independent spectral channels constituting an incoming spectrum. From an SNR perspective, this suggests a potential degradation of up to around 10 times, whereas for a sparse input spectrum, the SNR would become comparable to that of a conventional spectrometer. (see text S4 for comparative SNR analysis and fig. S14 for numerical results on reconstruction performance under a low photon budget scenario).

To conclude, we explored the use of double-layer disordered metasurfaces as a dispersive element for the spectrometer. In a broader term, the double-layer disordered configuration offers versatility to engineer the input-output relation in the spatio-spectral domain, which is formulated as a multispectral transmission matrix. Potentially, similar functionality could be achieved with a single metasurface, where nonlocal features of spatially extended modes across multiple nanostructures facilitate the in-plane mixing of spatial modes in a wavelength-dependent manner (*36*, *37*). By further incorporating input spatial degrees of freedom, the presented technology has the potential to serve as a key element for achieving on-sensor hyperspectral imaging and wavelength-multiplexed complex wavelength shaping for 3D light focusing and beam scanning. Also, considering that the spectral degrees of freedom can be transformed into the temporal degrees of freedom, temporally varying speckles can be specifically designed and used for ultrafast imaging or pulse shaper. Together, we anticipate that this unprecedented engineering flexibility will open up avenues for enabling unconventional imaging and light manipulation capabilities in the spatio-spectral and spatiotemporal domains.

MATERIALS AND METHODS

Design of disordered metasurface

Meta-atoms were composed of silicon nitride (SiN_x) nanoposts with a height of 630 nm with a periodic square lattice of 350 nm (*28*, *29*). The complex modulation functions of meta-atoms with a square cross section were determined by varying widths of meta-atoms for both horizontal and vertical polarizations, using the RCWA (*38*). A specific set of meta-atom widths was selected to induce phase delays ranging from 0 to 2π at 532 nm with nearly unity transmittance. The phase map of the disordered metasurface was designed using the Gerchberg-Saxton algorithm to generate a fully developed speckle while constraining the scattering profile to be uniformly distributed within a numerical aperture of 0.6, thereby preventing excessive light loss. The total area of the metasurface was set to 1 mm^2. The optimized phase map was converted into a meta-atom width map by substituting the phase values with corresponding meta-atom widths at each lattice point.

Fabrication of disordered metasurface

The aperture of 1 mm by 1 mm was fabricated on a fused silica substrate by transferring the pattern using photolithography and lift-off techniques, with layers of 10 nm Cr and 100 nm Au. A silicon nitride (SiN_x) film of 630-nm thickness was deposited above the aperture using plasma-enhanced chemical vapor deposition. The metasurface pattern was transferred within the aperture using e-beam lithography (EBL). The e-beam resist was developed, and a 60-nm-thick aluminum oxide (Al_2O_3) layer was deposited through e-beam evaporation. The resist was then stripped using resist remover. The resulting Al_2O_3 pattern on SiN_x was transformed into a SiN_x nanopost array by inductively coupled plasma reactive ion etching (ICP-RIE) using a mixture of C_4F_8 and SF_6 gases. The residual Al_2O_3 mask was removed using a mixture of NH_4OH and H_2O_2. Parameters such as dose for EBL and gas ratio, pressure, and power for ICP-RIE were fine-tuned by observing the results with scanning electron microscopy (SEM) and atomic force microscopy. To configure double-layer metasurfaces on a CMOS sensor (IMX178, Sony), the space between each element was filled with 3D-printed spacer molds and fixed using ultraviolet-cured resin.

Experimental setup for speckle measurement

Both a tunable laser (C-WAVE VIS, HÜBNER) and a supercontinuum laser (ROCK-500-6, LEUKOS) were used as the laser sources. The single-frequency laser line of the tunable laser was monitored by a wavemeter (AbsoluteLambda A3000, HÜBNER), measuring the wavelength of the optical parametric oscillator output, which is exactly double the wavelength of the second harmonic generation (SHG) output. The SHG output beam was used for the visible range single frequency laser source. The supercontinuum laser was first filtered by a hot mirror (M254H45, Thorlabs) to remove infrared spectra. Combinations of spectral filters (FGV9, NF533-17, NF561-18, FBH630-10, Thorlabs) were used to generate distinctive spectral fingerprints. Optical paths from both lasers were combined with a nonpolarizing beam splitter and coupled with a single-mode fiber (S405-XP, Thorlabs). The combined beam was collimated by an achromatic lens ($f = 50$ mm) and split into two paths by another nonpolarizing beam splitter. One of the beams was analyzed by our metasurface spectrometer and another beam was analyzed by conventional spectrometry. The conventional spectrometry was implemented by dispersing the spectrum with a transmissive grating (GT25-06 V, Thorlabs) and its first-order beam was focused on a CMOS (BFS-U3-120S4M-CS, FLIR) sensor by achromatic lens ($f = 50$ mm). The conventional spectrometer was calibrated by measuring five monochromatic waves (450 to 650 nm with 50-nm intervals) from the tunable laser. To characterize spectral sensitivity and degeneracy, the axial positions of metasurfaces were controlled by motorized actuators, while input monochromatic wavelength was controlled by the tunable laser.

To measure the speckle correlation profile over an entire visible spectrum, a fast-scanning narrowband monochromator (0.49-nm spectral linewidth at 600 nm) was built using a supercontinuum laser and a galvanometer mirror, as the tunable laser takes about 10 min to switch wavelengths. The monochromator was constructed by directing the supercontinuum laser onto a reflective grating (GR25-0605, Thorlabs) to disperse the light. The dispersed light was then directed onto a galvanometer mirror (GVS-001, Thorlabs) and an achromatic lens ($f = 150$ mm), which allowed a specific spectral band to pass through a 20-μm diameter pinhole. The selected light was finally coupled into a single-mode fiber. A fiber bench was used to guide a small portion of the monochromator output to an optical spectrum analyzer (OSA201C, Thorlabs) for spectrum monitoring. The monochromator output wavelength was controlled by adjusting a voltage signal from the DAQ board (PCIe-6323, NI) to the galvanometer mirror, with feedback from the spectrum analyzer to achieve the target wavelength.

Simulation of speckle output

Speckles were generated using the following the wave propagation model: Phase maps of all spectral channels were calculated from the meta-atom width map with wavelength-dependent phase delay function, which was derived by RCWA at each wavelength, while amplitude maps were assumed to have uniform distribution based on the close-to-unity transmittance of the RCWA result. The transmitted field U_1 after passing through the front metasurface is $U_1 = e^{i\varphi_1(\lambda)}$, where $\varphi_1(\lambda)$ is the phase map (with lateral coordinates omitted). Subsequently, the propagated fields $U_{1,T}$ were computed by the band-limited angular spectrum method (*39*). T indicates the thickness of the dispersive element. The field U_2 transmitted through the rear metasurface was computed by point-wise multiplication between the propagated field $U_{1,T}$ and the phase map of the rear metasurface: $U_2 = M_{mm}\left[U_{1,T}\right] \cdot e^{i\varphi_2(\lambda)}$, where $\varphi_2(\lambda)$ is the phase map of rear metasurface, and M_{mm} is shift and rotation operator that reflects the configuration between two metasurfaces. Again, propagated field $U_{2,L}$ to the image sensor was computed by the band-limited angular spectrum method. L indicates the element-to-sensor distance. After applying a shift and rotation operator M_{ms} to compensate to account for the configuration between the metasurface and sensor, it was transformed into an intensity map. Last, down-sampling from the periodic square lattice of 350 nm to the pixel size of the image sensor was conducted by applying the down-sampling operator D. The final outcome of the wave propagation model is $I_d = D\left[\left|M_{ms}\left[U_{2,L}\right]\right|^2\right]$, where I_d is the computer-generated speckle of double-layer disordered metasurfaces. For single metasurface, I_d was calculated using $U_{1,L}$ instead of $U_{2,L}$.

Determination of configurational parameters

The configurational parameters T, L, Δx_{mm}, Δy_{mm}, $\Delta\theta_{mm}$, $\Delta\theta_{ms}$ were determined using a global optimization algorithm (i.e., Bayesian optimization) to maximize the correlation coefficient between the measured speckle and the computer-generated speckle. Although a speckle pattern for this step can be acquired at an arbitrary wavelength, it was obtained at 620 nm for our experiments. We calculated the 2D cross-correlation between the measured and computer-generated speckles and used the correlation value as the objective function for the Bayesian optimization. The parameters

Δx_{ms}, Δy_{ms} were directly calculated from the position of the 2D cross-correlation peak.

Reconstruction of the spectrum

The spectrum $\mathbf{s}$ was reconstructed from the vectorized measured intensity $\mathbf{i}$. More specifically, the gradient descent optimization method with L1-norm and total variation (TV) norm was performed with a computer-generated spectral response matrix $\mathbf{W}$: $\hat{\mathbf{s}} = \underset{\mathbf{s}\geq\mathbf{0}}{argmin}\, \|\mathbf{i}-\mathbf{Ws}\|_2^2 + \gamma_1\|\mathbf{s}\|_1 + \gamma_2\|\boldsymbol{\Psi}\mathbf{s}\|_1$, where γ_1 is the tuning parameter modulating L1-norm regularization $\|\mathbf{s}\|_1$, γ_2 is the tuning parameter modulating TV norm regularization $\|\boldsymbol{\Psi}\mathbf{s}\|_1$, and $\boldsymbol{\Psi}$ is the matrix for computing TV. γ_1 and γ_2 are tuned to have maximized correlation between the reconstructed spectrum and the original spectrum.

Supplementary Materials

This PDF file includes:

Supplementary Text S1 to S4
Figs. S1 to S14

REFERENCES AND NOTES

1. Z. Yang, T. Albrow-Owen, W. Cai, T. Hasan, Miniaturization of optical spectrometers. *Science* **371**, eabe0722 (2021).
2. R. Cheng, C.-L. Zou, X. Guo, S. Wang, X. Han, H. X. Tang, Broadband on-chip single-photon spectrometer. *Nat. Commun.* **10**, 4104 (2019).
3. M. Faraji-Dana, E. Arbabi, A. Arbabi, S. M. Kamali, H. Kwon, A. Faraon, Compact folded metasurface spectrometer. *Nat. Commun.* **9**, 4196 (2018).
4. T. Yokino, K. Kato, A. Ui, S. Nakata, T. Suzuki, R. Abe, S. Suzuki, Y. Warashina, K. Shibayama, K. Yamamoto, "Grating-based ultra-compact SWNIR spectral sensor head developed through MOEMS technology," in *MOEMS and Miniaturized Systems XVIII* (SPIE, 2019), vol. 10931, pp. 55–68; https://spiedigitallibrary.org/conference-proceedings-of-spie/10931/1093108/Grating-based-ultra-compact-SWNIR-spectral-sensor-head-developed-through/10.1117/12.2510472.short.
5. A. Y. Zhu, W.-T. Chen, M. Khorasaninejad, J. Oh, A. Zaidi, I. Mishra, R. C. Devlin, F. Capasso, Ultra-compact visible chiral spectrometer with meta-lenses. *APL Photonics* **2**, 036103 (2017).
6. N. Neumann, M. Ebermann, S. Kurth, K. Hiller, Tunable infrared detector with integrated micromachined Fabry-Perot filter. *J. Micro. Nanolithogr. Microfab. Microsys.* **7**, 021004 (2008).
7. A. Nitkowski, L. Chen, M. Lipson, Cavity-enhanced on-chip absorption spectroscopy using microring resonators. *Opt. Express, OE* **16**, 11930–11936 (2008).
8. A. Tittl, A. Leitis, M. Liu, F. Yesilkoy, D.-Y. Choi, D. N. Neshev, Y. S. Kivshar, H. Altug, Imaging-based molecular barcoding with pixelated dielectric metasurfaces. *Science* **360**, 1105–1109 (2018).
9. D. M. Kita, B. Miranda, D. Favela, D. Bono, J. Michon, H. Lin, T. Gu, J. Hu, High-performance and scalable on-chip digital Fourier transform spectroscopy. *Nat. Commun.* **9**, 4405 (2018).
10. O. Manzardo, H. P. Herzig, C. R. Marxer, N. F. de Rooij, Miniaturized time-scanning Fourier transform spectrometer based on silicon technology. *Opt. Lett.* **24**, 1705–1707 (1999).
11. D. Pohl, M. Reig Escalé, M. Madi, F. Kaufmann, P. Brotzer, A. Sergeyev, B. Guldimann, P. Giaccari, E. Alberti, U. Meier, R. Grange, An integrated broadband spectrometer on thin-film lithium niobate. *Nat. Photonics* **14**, 24–29 (2020).
12. Z. Wang, S. Yi, A. Chen, M. Zhou, T. S. Luk, A. James, J. Nogan, W. Ross, G. Joe, A. Shahsafi, K. X. Wang, M. A. Kats, Z. Yu, Single-shot on-chip spectral sensors based on photonic crystal slabs. *Nat. Commun.* **10**, 1020 (2019).
13. J. Bao, M. G. Bawendi, A colloidal quantum dot spectrometer. *Nature* **523**, 67–70 (2015).
14. Z. Yang, T. Albrow-Owen, H. Cui, J. Alexander-Webber, F. Gu, X. Wang, T.-C. Wu, M. Zhuge, C. Williams, P. Wang, A. V. Zayats, W. Cai, L. Dai, S. Hofmann, M. Overend, L. Tong, Q. Yang, Z. Sun, T. Hasan, Single-nanowire spectrometers. *Science* **365**, 1017–1020 (2019).
15. Z. Wang, Z. Yu, Spectral analysis based on compressive sensing in nanophotonic structures. *Opt. Express* **22**, 25608–25614 (2014).
16. P. Wang, R. Menon, Computational spectrometer based on a broadband diffractive optic. *Opt. Express* **22**, 14575–14587 (2014).
17. B. Redding, M. Alam, M. Seifert, H. Cao, High-resolution and broadband all-fiber spectrometers. *Optica* **1**, 175–180 (2014).
18. B. Redding, S. Fatt Liew, Y. Bromberg, R. Sarma, H. Cao, Evanescently coupled multimode spiral spectrometer. *Optica* **3**, (2016).
19. B. Redding, S. F. Liew, R. Sarma, H. Cao, Compact spectrometer based on a disordered photonic chip. *Nat. Photonics* **7**, 746–751 (2013).
20. J. D. Malone, N. Aggarwal, L. Waller, A. K. Bowden, DiffuserSpec: Spectroscopy with scotch tape. *Opt. Lett.* **48**, 323–326 (2023).
21. W. Hartmann, P. Varytis, H. Gehring, N. Walter, F. Beutel, K. Busch, W. Pernice, Waveguide-integrated broadband spectrometer based on tailored disorder. *Adv. Opt. Mater.* **8**, 1901602 (2020).
22. Z. Lin, S. Yu, Y. Chen, W. Cai, B. Lin, J. Song, M. Mitchell, M. Hammood, J. Jhoja, N. A. F. Jaeger, W. Shi, L. Chrostowski, High-performance, intelligent, on-chip speckle spectrometer using 2D silicon photonic disordered microring lattice. *Optica* **10**, 497–504 (2023).
23. N. K. Metzger, R. Spesyvtsev, G. D. Bruce, B. Miller, G. T. Maker, G. Malcolm, M. Mazilu, K. Dholakia, Harnessing speckle for a sub-femtometre resolved broadband wavemeter and laser stabilization. *Nat. Commun.* **8**, 15610 (2017).
24. M. Chakrabarti, M. L. Jakobsen, S. G. Hanson, Speckle-based spectrometer. *Opt. Lett.* **40**, 3264–3267 (2015).
25. G. D. Bruce, L. O'Donnell, M. Chen, K. Dholakia, Overcoming the speckle correlation limit to achieve a fiber wavemeter with attometer resolution. *Opt. Lett.* **44**, 1367–1370 (2019).
26. A. P. Mosk, A. Lagendijk, G. Lerosey, M. Fink, Controlling waves in space and time for imaging and focusing in complex media. *Nat. Photonics* **6**, 283–292 (2012).
27. L. Zhu, J. Boutet de Monvel, P. Berto, S. Brasselet, S. Gigan, M. Guillon, Chromato-axial memory effect through a forward-scattering slab. *Optica* **7**, 338–345 (2020).
28. M. Jang, Y. Horie, A. Shibukawa, J. Brake, Y. Liu, S. M. Kamali, A. Arbabi, H. Ruan, A. Faraon, C. Yang, Wavefront shaping with disorder-engineered metasurfaces. *Nat. Photonics* **12**, 84–90 (2018).
29. A. Arbabi, Y. Horie, A. J. Ball, M. Bagheri, A. Faraon, Subwavelength-thick lenses with high numerical apertures and large efficiency based on high-contrast transmitarrays. *Nat. Commun.* **6**, 7069 (2015).
30. B. Redding, S. M. Popoff, H. Cao, All-fiber spectrometer based on speckle pattern reconstruction. *Opt. Express* **21**, 6584–6600 (2013).
31. J. W. Goodman, *Speckle Phenomena in Optics: Theory and Applications* (Roberts and Company Publishers, 2007).
32. J. C. Dainty, *Laser Speckle and Related Phenomena* (Springer science & business Media, 2013), vol. 9.
33. S. Feng, C. Kane, P. A. Lee, A. D. Stone, Correlations and fluctuations of coherent wave transmission through disordered media. *Phys. Rev. Lett.* **61**, 834–837 (1988).
34. I. Freund, M. Rosenbluh, S. Feng, Memory effects in propagation of optical waves through disordered media. *Phys. Rev. Lett.* **61**, 2328–2331 (1988).
35. S. M. Kamali, A. Arbabi, E. Arbabi, Y. Horie, A. Faraon, Decoupling optical function and geometrical form using conformal flexible dielectric metasurfaces. *Nat. Commun.* **7**, 11618 (2016).
36. F. Tang, J. Wu, T. Albrow-Owen, H. Cui, F. Chen, Y. Shi, L. Zou, J. Chen, X. Guo, Y. Sun, J. Luo, B. Ju, J. Huang, S. Liu, B. Li, L. Yang, E. A. Munro, W. Zheng, H. J. Joyce, H. Chen, L. Che, S. Dong, Z. Sun, T. Hasan, X. Ye, Y. Yang, Z. Yang, Metasurface spectrometers beyond resolution-sensitivity constraints. *Sci. Adv.* **10**, eadr7155 (2024).
37. G. Cai, Y. Li, Y. Zhang, X. Jiang, Y. Chen, G. Qu, X. Zhang, S. Xiao, J. Han, S. Yu, Y. Kivshar, Q. Song, Compact angle-resolved metasurface spectrometer. *Nat. Mater.* **23**, 71–78 (2024).
38. J. P. Hugonin, P. Lalanne, RETICOLO software for grating analysis. arXiv:2101.00901 [physics.optics] (2025); https://doi.org/10.48550/arXiv.2101.00901.
39. K. Matsushima, T. Shimobaba, Band-limited angular spectrum method for numerical simulation of free-space propagation in far and near fields. *Opt. Express* **17**, 19662–19673 (2009).

Acknowledgments

Funding: This work was supported by Samsung Research Funding and Incubation Center of Samsung Electronics grant SRFC-IT2002-03 (M.J., D.L., G.S., Chunghyung Lee, and Chanseok Lee), National Research Foundation of Korea grant funded by the Korean government grant NRF-2021R1C1C1011307 (M.J., D.L., G.S., Chunghyung Lee, and Chanseok Lee), National Research Foundation of Korea grant funded by the Korean government grant NRF-RS-2021-NR060086 (M.J., D.L., G.S., Chunghyung Lee, and Chanseok Lee), and Bio&Medical Technology Development Program of the National Research Foundation funded by the Korean government grant RS-2024-00397673 (M.J., D.L., G.S., Chunghyung Lee, and Chanseok Lee). **Author contributions:** Conceptualization: M.J., G.S., and D.L. Experiments: G.S. and D.L. Device fabrication: D.L. Data analysis: G.S., D.L., Chunghyung Lee, and Chanseok Lee. Writing—original draft: D.L. and G.S. Writing—review and editing: M.J., D.L., and G.S. Supervision: M.J. **Competing interests:** M.J., G.S., Chunghyung Lee, and D.L. are inventors on a provisional patent application related to this work to be filed by KAIST (no. 18/598,372). M.J., G.S., and D.L. are inventors on another provisional patent application related to this work to be filed by KAIST (no. 18/443,488). The authors declare that they have no other competing interests. **Data and materials availability:** All data needed to evaluate the conclusions in the paper are present in the paper and/or the Supplementary Materials.

Submitted 10 December 2024
Accepted 23 April 2025
Published 28 May 2025
10.1126/sciadv.adv2376